PAPER

Helicon normal modes in Proto-MPEX

View the article online for updates and enhancements.

Helicon normal modes in Proto-MPEX*

P A Piotrowicz[1,2,3] ⓘ, **J F Caneses**[1] ⓘ, **D L Green**[1], **R H Goulding**[1], **C Lau**[1] ⓘ, **J B O Caughman**[1], **J Rapp**[1] ⓘ and **D N Ruzic**[2]

[1] Oak Ridge National Laboratory, Oak Ridge, TN, United States of America
[2] University of Illinois Urbana-Champaign, Urbana, IL, United States of America

E-mail: ppiotr3@illinois.edu and canesesmarjf@ornl.gov

CrossMark

Abstract

The Proto-MPEX helicon source has been operating in a high electron density 'helicon-mode'. Establishing plasma densities and magnetic field strengths under the antenna that allow for the formation of normal modes of the fast-wave are believed to be responsible for the 'helicon-mode'. A 2D finite-element full-wave model of the helicon antenna on Proto-MPEX is used to identify the fast-wave normal modes responsible for the steady-state electron density profile produced by the source. We also show through the simulation that in the regions of operation in which core power deposition is maximum the slow-wave does not deposit significant power besides directly under the antenna. In the case of a simulation where a normal mode is not excited significant edge power is deposited in the mirror region.

Keywords: MPEX, plasma source, plasma waves, helicon source, full wave simulation, deuterium

1. Introduction

Ever since Boswell published on the ionization efficiency of inductively coupling RF waves to the natural oscillations in a plasma column [1, 2], helicon plasma sources have gained interest in many applications. A recent application of helicon sources has been as plasma sources for fusion-relevant plasma-material interactions (PMI) investigation [3–8]. However, in order for helicon sources to be relevant to PMI investigation, they must be able to produce high-density plasmas with light ion fuels (H_2, D_2, He). In this paper we will use a 2D finite element model to identify helicon normal modes excited in the Prototype Materials Plasma Exposure eXperiment (Proto-MPEX) device [8, 9] during the high-density 'helicon-mode' operation.

Light ion helicon sources have proven more difficult to achieve high-density plasmas with [10, 11] than heavy ion helicon sources. Sakawa [10] showed that for a helicon source

fueled with D_2 and H_2 gas, electron density would reach a maximum at $B_0 \approx 0.02$ T then sharply fall off. This is not the case using Ar gas to fuel the discharge, which would show a linear increase in electron density past $B_0 = 0.15$ T. That work then showed that the reduced ion mass moves the high-density limit of the lower hybrid resonance (HDLH), which reduces to the root of the product of the electron and ion cyclotron frequencies as $\omega_{HDLH} = \sqrt{\omega_{ce}\omega_{ci}}$, to lower magnetic field values. Operating in magnetic field values above the HDLH, $B_0 \gtrsim 0.02$ T for D_2, restricts the slow-wave to the low electron density region of the plasma column and the helicon wave to the high-density region, thus creating a region in the plasma that is evanescent to both waves. Light and Chen [11] later showed that low-frequency instabilities that have characteristics of the resistive drift wave instability and the Kelvin–Helmholtz instability were more prevalent in plasmas with light ion mass operating above the HDLH.

Several devices have been able to achieve high electron densities in light ion plasmas [7–9, 12, 13] operating in magnetic fields above the HDLH. These devices all used a converging magnetic field geometry. However, the effect of this magnetic geometry on the success of these devices is not understood. Mori [12] measured fast-wave radial normal modes on the mini-RFTF devices and attributed their excitation to the variation of electron density with the magnetic field. On the Proto-MPEX device, the 'helicon-mode' is

attributed to exciting radial normal modes of the fast-wave in the plasma column [8, 9].

Identifying the physical mechanisms of power deposition of the fast-wave in helicon sources has been a point of interest in literature [14–20]. Most authors attribute the efficient ionization of helicon sources in heavy ion discharges to the collisional damping of the Trivelpiece Goulde mode (TG) [16, 21–24]. The TG mode, slow-wave, is typically excited through non-resonant mode conversion of the helicon-mode, fast-wave, that occurs at the periphery of the plasma [25], therefore power deposition is typically edge dominated in helicon sources using heavy ions. Chen and Curreli [23, 24] have shown that regardless of where the ionization occurs, the centrally peaked profile in heavy ion helicon discharges can be explained by the short circuit effect. The short circuit effect is restricted to short discharges with unmagnetized ions. In discharges using light ions, this effect is then typically not applicable and hollow density profiles are observed when significant core power deposition is not observed [9]. For this reason, authors that describe wave physics on light ion devices focus on the damping of the fast-wave and its formation of radial normal modes [7, 12, 13, 26].

In this work, we will describe a 2D axisymmetric model used to identify the fast-wave normal modes in Proto-MPEX that are responsible for the 'helicon-mode'. In section 2 we will describe the physics of fast-wave normal modes and relate this to the increased core power deposition observed. In section 3 the experimental conditions and observations during the 'helicon-mode' are reported. Section 4 describes the computational model used to identify the radial normal modes in Proto-MPEX. Section 5 presents the results of the modeling and includes a discussion on them. Concluding remarks and discussion on possible ways to optimize light ion helicon operations are presented in section 6.

2. Helicon normal modes

Resonant matching of the fast-wave wavenumber with the eigenmode solutions of a uniform plasma column surrounded by an electrical conductor was discussed in the early years of the theoretical development of the wave physics and discussed in great detail by Shamrai [27]. However, follow up work [21] discusses how the introduction of a vacuum gap of sufficient size between the plasma column and the electrical conductor removes the resonance observed in the earlier theory. An interesting phenomenon that appears in this analytical treatment of the plasma discharge is the anti-resonant behavior of the slow-wave; which predicts a condition where the amplitude of the slow-wave goes to zero. In this condition, [21] shows that the RF fields of the slow-wave in a plasma column that satisfies the anti-resonance condition are reduced. Therefore, a slow-wave anti-resonance results in a reduction in edge power deposition which allows for more energy available to the fast-wave and increased core power deposition. In a more complicated picture of a plasma column with a density gradient, the slow-wave anti-resonance can be understood as a reduction of non-resonant mode conversion by the reduction of the fast-wave amplitude at the edge of
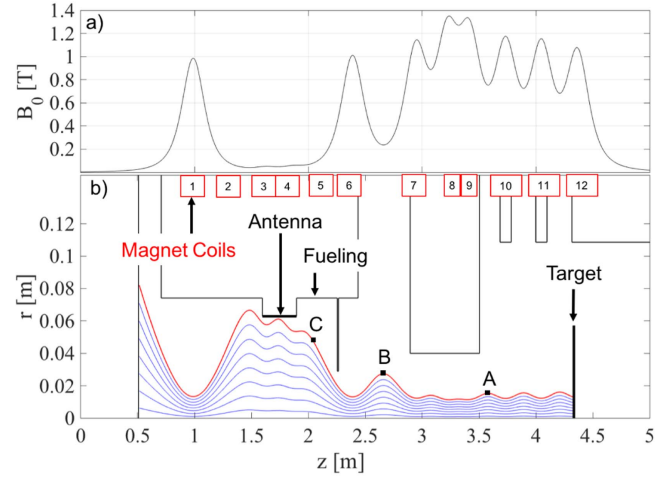

Figure 1. (a) On-axis magnetic field strength in Proto-MPEX for $I_H = 160$ A. (b) Flux line mapping and two dimensional schematic of Proto-MPEX with the locations of the helicon antenna, gas fueling, and locations of electron density measurements made with double Langmuir probes are shown.

the plasma column. This process is explained in [25] and can be summed up by $|E_r^{TG}|_{R_p} = \omega_{ce}\omega^{-1}|E_\theta^H|_{R_p}$, where R_p is the plasma radius, E_θ^H is the azimuthal component of the fast-wave's electric field, E_r^{TG} is the radial component of the slow-wave's electric field.

The bounded dispersion relation given by equation (1) predicts both the normal modes of the fast-wave and the TG anti-resonant mode. Therefore, we will refer to a discharge in which the tangential $\vec{B}$ component of the fast-wave satisfies equation (1) as a fast-wave normal mode.

$$J_m'(k_- R_p) + \frac{m}{k_z R_p}J_m(k_- R_p) = 0, \tag{1}$$

$$k_- = \frac{\omega_{pe}^2 k_0^2}{\omega\omega_{ce}k_z}, \tag{2}$$

where J_m and J_m' is the Bessel function and its derivative, m is the azimuthal mode number, k_z is the axial wavenumber, k_0 is the vacuum wavenumber, ω is the driving frequency, ω_{pe} is the plasma frequency, ω_{ce} is the electron cyclotron frequency, and R_p is the plasma radius. Simplifying equation (1) using the long wavelength approximation ($k_z R_p \leqslant 1$) gives a convenient form that allows writing the electron density as a function of the magnetic field as.

$$n_e = \frac{c^2\epsilon_0}{q}\left(\frac{B_0 k_z}{\omega R_p}\right)\left(p_{mi} - \frac{k_z R_p}{m}\right). \tag{3}$$

Equation (3) predicts a linear dependence of electron density (n_e) to the background magnetic field (B_0). However, the slope of this linear behavior is determined by the radial mode number (p_{mi}) given by the *i*th root of the Bessel function. The axial wavenumbers and azimuthal modes are driven by the antenna geometry and these parameters along with the driving frequency will influence the coupling of fast-wave power to the plasma column. The antenna geometry is a right-handed partial-turn helical antenna. The spectrum from this antenna is shown in figure 4, the total spectrum ($m = \pm 1$) is symmetric around k_z.
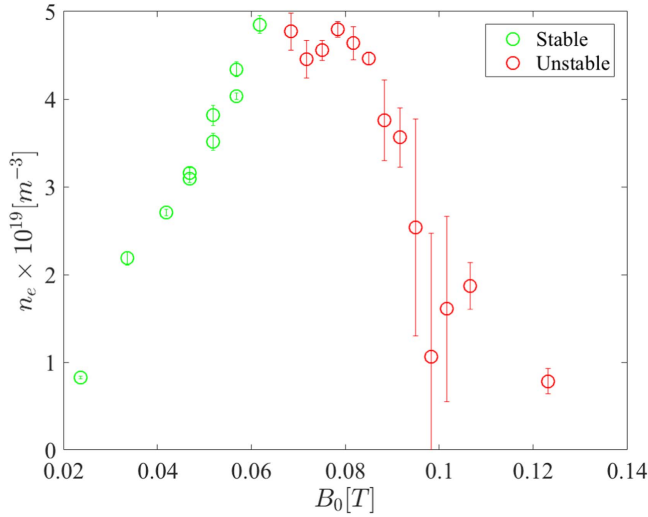
Figure 2. On-axis plasma density versus magnetic field strength under the helicon antenna. The plasma density is measured at the location A shown in figure 1.

However, the $m = +1$ mode of a right-handed antenna preferentially excites waves with positive k_z and the $m = -1$ mode preferentially excites waves with negative k_z. The electron density profile used throughout this work is described in section 4.2. It is described as a function of the magnetic flux coordinate. The axial variation of this coordinate can be seen in figure 1.

3. Experimental observations

The helicon antenna installed on Proto-MPEX is a 25 cm long by 15 cm diameter partial helix antenna powered by radio frequency (RF) power of up to 120 kW at a driving frequency of 13.56 MHz. The helicon antenna surrounds an aluminum nitride vacuum window with an inner radius located at 6.3 cm. There are 12 magnet coils available on Proto-MPEX, their axial locations are shown and labeled in figure 1. The configuration of the magnets is as follows; the mirror magnets (I_B) are coils 1, and 6–12, the supplemental magnets (I_0) are coils 2 and 5, and the helicon magnets (I_H) are coils 3 and 4. The location of the target is also shown in figure 1. The mirror magnets and supplemental magnets are held constant at $I_B = 5900$ A and $I_0 = 0$ A respectively. The helicon magnets are then varied to produce the reported fields in figure 2.

Neutral gas fueling of the plasma source is a critical component in successfully operating the helicon source. The high-density 'helicon-mode' was not observed in Proto-MPEX until neutral gas fueling was optimized. For the configuration considered in this paper, gas fueling of the discharge is 20 cm away from the helicon antenna and is labeled in figure 1. The fueling procedure is as follows: D_2 gas is injected at a flow rate of 2 standard liters per minute (SLM) beginning 300 ms before the RF pulse. At 50 ms before the RF pulse the flow rate is reduced to 0.5 SLM. Figure 1(b) shows the schematic of Proto-MPEX depicting the locations of the helicon antenna, gas fueling, and the double Langmuir

probes (A, B, and C) used to report electron density data. The contours on the device schematic show the magnetic flux lines (blue) up to the flux line limited by the helicon window (red) for $I_H = 160$ A. Figure 1(a) shows the on-axis magnetic field strength down the device for this magnetic field configuration.

High-density operation of the helicon antenna on Proto-MPEX has been recently observed [8, 9] and is referred to as the 'helicon-mode'. This mode of operation is characterized by an increase in on-axis electron density from 2×10^{19} to 6×10^{19} m^{-3}, transition from a hollow to centrally peaked electron density profile, transition from hollow to a flat electron temperature profile, and substantial increase in core power coupling as observed from IR thermography. More details on the 'helicon-mode' and its characteristics can be found in [8, 9]. The 'helicon-mode' plasma is observed to be a stable plasma over the entire pulse length. When the plasma does not enter the 'helicon-mode' the plasma is noisy and low-frequency oscillations of electron density and temperature are observed on the double Langmuir probes, as is evident by the error-bars in figure 2.

The nature of these instabilities has not yet been explored in this device. However, the timescale of the instabilities is similar to those observed and characterized by Light [11]. Another possible source of the instability could be due to neutral depletion and the relaxation oscillations Degeling observed and described [28, 29]. Throughout this paper, the focus will be on characterizing the antenna coupling to the stable modes of the plasma. These modes exhibit a linear behavior of electron density with magnetic field strength as shown in figure 2.

4. Full wave model

Maxwell's equations are solved in the frequency domain using the finite element analysis software COMSOL Multiphysics. The frequency domain wave equation solved is given by equation (4).

$$\nabla \times (\nabla \times \vec{E}) - k_0^2 \overset{\leftrightarrow}{\epsilon_r} \vec{E} = 0. \tag{4}$$

A 2D axisymmetric geometry is used and the RF Electric field is solved for assuming $m = +1$ symmetry where the fields vary as $\vec{E}(r, \phi, z) = \vec{E}(r, z)\mathrm{e}^{-\mathrm{i}m\phi}$. The $m = +1$ mode is the dominant azimuthal mode excited by a right-handed helical antennas [30, 31] with a magnetic field oriented in $+\hat{z}$, therefore the paper will focus on the $m = +1$ azimuthal mode for the analysis of the plasma wave physics.

4.1. Cold plasma model

The plasma is represented as a dielectric tensor ($\overset{\leftrightarrow}{\epsilon_r}$) derived from cold plasma theory [32] assuming $\vec{B}_0 = B_0\hat{z}$, this assumption is not valid in the Proto-MPEX magnetic geometry where strong gradients in the magnetic field result in significant curvature of the field lines. This is accounted for

by rotating the dielectric tensor to the orientation of the magnetic field lines using the rotation matrix ($\overset{\leftrightarrow}{Q}$) to rotate the STIX tensor ($\overset{\leftrightarrow}{K}$) by the angle ($\Psi$) between the magnetic field and the axial coordinate $\hat{z}$.

$$\overset{\leftrightarrow}{\epsilon}_r = \overset{\leftrightarrow}{Q}\,\overset{\leftrightarrow}{K}\,\overset{\leftrightarrow}{Q}^T, \tag{5}$$

$$\overset{\leftrightarrow}{K} = \begin{bmatrix} S & -\mathrm{i}D & 0 \\ \mathrm{i}D & S & 0 \\ 0 & 0 & P \end{bmatrix}, \tag{6}$$

$$\overset{\leftrightarrow}{Q} = \begin{bmatrix} \cos(\Psi) & 0 & \sin(\Psi) \\ 0 & 1 & 0 \\ -\sin(\Psi) & 0 & \cos(\Psi) \end{bmatrix}, \tag{7}$$

$$\Psi = \tan^{-1}\left(\frac{B_r}{B_z}\right). \tag{8}$$

Damping of the wave is approximated by the Krook model [32] which is implemented by a collision frequency ν modifying the mass of the electrons as $m_{e_{\mathrm{eff}}} = m_e(1 - \mathrm{i}\nu\omega^{-1})$. The effect of ν on the eigenmodes is discussed in section 5 of this paper.

4.2. Plasma density profile

The model geometry represents a 2D axisymmetric slice of Proto-MPEX. The magnetic field is calculated by solving Ampere's law from the geometry and current configuration of the magnetic field coils. The density is then implemented as a function of the radial coordinate and the azimuthal component of the magnetic vector potential ($A_\phi r$) whose contours correspond to the magnetic field lines in the geometry. The limiting flux line ($A_{\phi_{\mathrm{LF}}}R$) is defined by the smallest value of the magnetic flux that intersects the chamber wall near the helicon region. The electron density is then defined as a function of χ.

$$n_e = \begin{cases} n_{e_{\mathrm{peak}}}(1 - \chi^a)^b + n_{e_{\mathrm{edge}}} & \chi \leqslant 1 \\ n_{e_{\mathrm{edge}}} & \chi > 1, \end{cases} \tag{9}$$

$$\chi = \frac{A_\phi r}{A_{\phi_{\mathrm{LF}}}R}. \tag{10}$$

The peak electron density ($n_{e_{\mathrm{peak}}}$) and the current imposed on the helicon magnet coils (I_H) is scanned over experimentally relevant conditions while the edge density is held constant at $n_{e_{\mathrm{edge}}} = 10^{16}\,\mathrm{m}^{-3}$ throughout the analysis. The constants controlling the density profile in equation (9) are set to $a = 2$ and $b = 1.75$. Figure 3 shows equation (9) plotted against experimentally measured radial scans of electron density profiles measured at location A, B, and C. The experimental radial scans are converted to the χ coordinate based on calculated A_ϕ. The electron density is normalized to a peak density value in each measurement set. Axial variation of ($n_{e_{\mathrm{peak}}}$) is not imposed since it is not clear how this varies in the experiment under the helicon antenna.

Figure 3 compares normalized experimentally measured electron density profiles (the radial variation is normalized to the flux coordinate χ) with the function given by equation (9). These density profiles were measured at axial positions
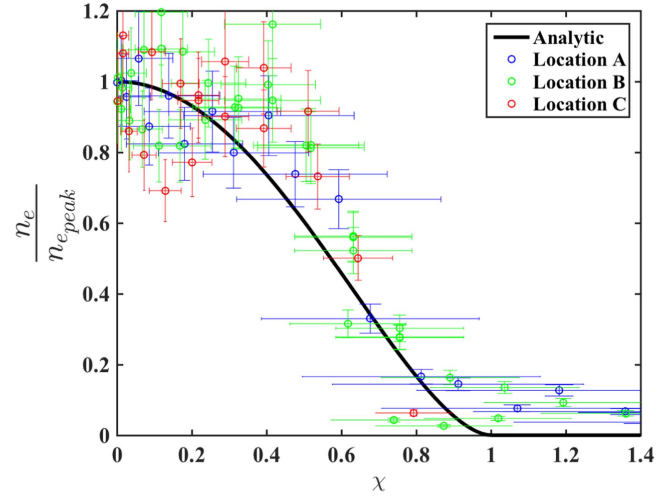

Figure 3. Normalized experimentally measured radial scans of electron density at location A, B, and C versus the electron density profile given by equation (9) with $a = 2$, $b = 1.75$, and $n_{e_{\mathrm{peak}}} = 1$. The radius of the experimentally measured radial scans is converted to $\chi = A_\phi r (A_{\phi_{\mathrm{LF}}} R)^{-1}$.

(locations A, B, and C in figure 1) where the background magnetic field is different. When plotted in magnetic flux coordinates, the radial profiles are self-similar. We note that the solid line representing our density model is not a fit to this data, but merely a representative function used to capture the flux expansion of the electron density profile.

4.3. Antenna description

The helicon antenna is described by a current imposed on a boundary at the radial location of the antenna. The current in physical space is described as a combination of the transverse current straps and the helical strap of the antenna [33]. The component of the transverse current strap is given by equation (11).

$$J_\phi^T = \frac{I_0}{2}(R_1(u_{\phi 1} + u_{\phi 2}) + R_2(u_{\phi 3} + u_{\phi 4})). \tag{11}$$

The first term in equation (11) describes the current ring closer to the target, and the second term describes the current ring further from the target. The current rings are described as boxcar functions in the azimuthal coordinate ϕ and in the axial coordinate z_a whose origin is at the geometric center of the antenna.

$$R_1(z_a) = H\left(\frac{L_a}{2}, \frac{L_a}{2} - R_w\right), \tag{12}$$

$$R_2(z_a) = H\left(\frac{-L_a}{2} + R_w, -\frac{L_a}{2}\right), \tag{13}$$

$$u_{\phi 1} = +H(\theta, \theta + \pi), \tag{14}$$

$$u_{\phi 2} = -H(\theta - \pi, \theta), \tag{15}$$

$$u_{\phi 3} = +H(-\theta - \pi, -\theta), \tag{16}$$

$$u_{\phi 4} = -H(-\theta, -\theta + \pi). \tag{17}$$

In equations (11) through (17) the I_0 is the antenna current, L_a is the antenna length, R_w is the width of the transverse current strap, and θ is proportional to the number of helical turns (l) of the antenna ($\theta = \pi$ l). The square function ($H(x)$) has properties such that:

$$H(a, b) = \begin{array}{ll} 1 & a < x < b \\ 0 & \text{otherwise.} \end{array} \qquad (18)$$

The azimuthal component of the current (J_ϕ) on the helical strap is described as:

$$J_\phi^H = I_0 \left(\delta \left(z_a + \frac{L_a}{2\theta} \phi \right) + \delta \left(z_a + \frac{L_a}{2\theta} (\phi - \pi) \right) \right). \qquad (19)$$

The azimuthal Fourier transform of the transverse and helical current straps is then given by:

$$\bar{J}_\phi^T = \frac{I_0}{2} \frac{4\mathrm{i}}{m\sqrt{2\pi}} (-R_1 \mathrm{e}^{-\mathrm{i}m\theta} + R_2 \mathrm{e}^{\mathrm{i}m\theta}), \qquad (20)$$

$$\bar{J}_\phi^H = 2\theta \frac{I_0}{L_a} \sqrt{\frac{2}{\pi}} \, \mathrm{e}^{\frac{2\mathrm{i}m\theta z_a}{L_a}}. \qquad (21)$$

The total azimuthal current of the antenna is then given by the contribution from the helical strap and the two transverse straps. To define the axial current of the helical strap we can use the divergence-free condition ($\nabla \cdot \vec{J} = 0$) which results in the following definition for the axial current.

$$\bar{J}_z = -\frac{\mathrm{i}m}{R} \int \bar{J}_\phi^H \, \mathrm{d}z. \qquad (22)$$

This integration then yields:

$$\bar{J}_z = -\frac{I_0}{R} \sqrt{\frac{2}{\pi}} \, \mathrm{e}^{\frac{2\mathrm{i}m\theta z_a}{L_a}}. \qquad (23)$$

Equations (20), (21) and (23) are then used in the 2D axisymmetric simulation to describe the antenna. The vacuum spectrum of the antenna from the 2D simulation with both $m = \pm 1$ modes was compared to a COMSOL 3D simulation with real antenna geometry and a self-consistent antenna current. Figure 4 shows the comparison of the vacuum spectra from the 2D and 3D simulations. In the 2D simulation, a damping term was added in the region where the antenna current was defined for numerical stability of the solution. Because of this damping term, the power deposition from the 2D simulation will be reported as normalized. However, this should not affect the results reported herein as the field amplitude will scale linearly with increasing power and the field profiles are not affected.

4.4. Dispersion analysis

To interpret the results of full wave simulations it is important to understand the dispersive properties of the waves propagating in the plasma. The cold plasma dispersion relation can be written for the perpendicular wavenumber as a function of the parallel wavenumber, electron density, magnetic field strength, and the driving frequency [32]. The expected parallel wavenumber propagating in the plasma can be estimated by the vacuum spectrum of the antenna [34] which is shown in figure 4. The driving frequency, electron density, and magnetic field strength are all inputs into the electromagnetic
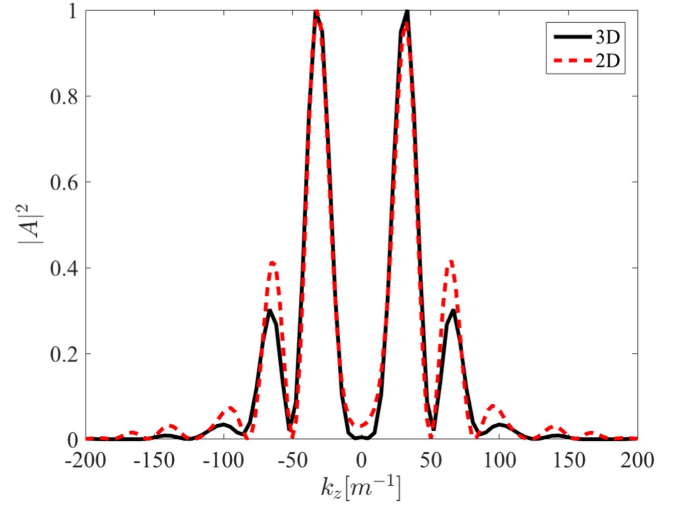

Figure 4. Comparison of the Fourier components of the vacuum B_z from the 2D axisymmetric simulation using both the $m = +1$ and $m = -1$ modes of the antenna spectrum with a 3D self-consistent simulation of the helicon antenna.

simulation. Figure 5 shows contours of where the perpendicular wavelength of the slow-wave (red) and the fast-wave (blue) is real. These are solved assuming a parallel wavelength of $k_z = 20 \text{ m}^{-1}$, a driving frequency of $\omega = 13.56 \text{ MHz}$, an electron density defined by equation (9) using $n_{e_{\text{peak}}} = 2.7 \times 10^{19} \text{ m}^{-3}$, and the magnetic field is calculated from Ampere's law from the magnetic coil geometry described in section 3 with $I_H = 260 \text{ A}$.

From figure 5 it is clear that the fast-wave does not propagate past the magnetic mirror region and is contained to the high electron density region $n_e > 1 \times 10^{18} \text{ m}^{-3}$. The slow-wave is contained to the low electron density region ($n_e < 1 \times 10^{16}$) m^{-3} of the plasma column. The slow-wave encounters the lower hybrid resonance along the electron density gradient and therefore does not propagate inside the plasma column. The fast-wave encounters a cut-off where $k_\perp = 0$ along the electron density gradient and along the magnetic field gradient. This cut-off along the magnetic field gradient restricts the fast-wave to the region between the magnetic mirrors and effectively creates a cavity for the fast-wave.

5. Results and discussion

In section 5.1 the effect of the collision frequency (ν) on the normal mode behavior is presented and discussed. In section 5.2 the experimentally relevant normal modes, which are identified as points of maximum core power deposition, are compared to solutions where the helicon antenna does not excite normal modes, which are identified as points of minimum core power deposition. In section 5.3 a discussion of the RF fields for a simulation with parameters that give rise to increased core power deposition are compared to the simulation with parameters where core power deposition is minimal. Section 5.4 will show 2D power deposition contours for both cases described above.
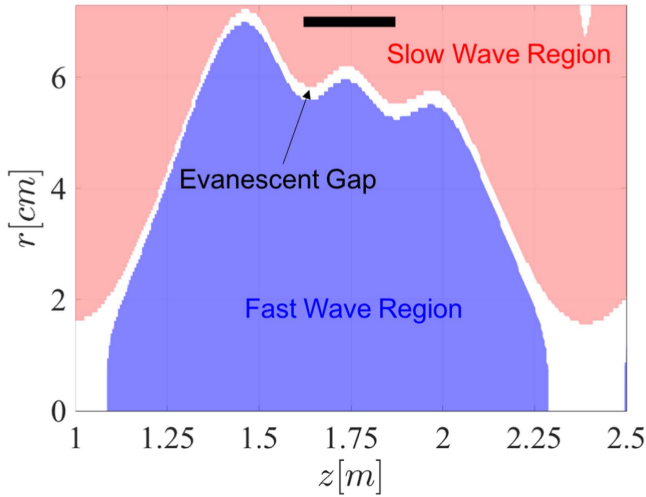
Figure 5. Contours of perpendicular wavelength ($k_\perp$) solved for from the cold plasma dispersion relation assuming $k_z = 20$ m^{-1} and electron density defined by equation (9) using $n_{e_{peak}} = 2.7 \times 10^{19}$ m^{-3}. The magnetic field is solved for with $I_H = 260$ A. The blue contour represents where $k_\perp$ for the fast-wave solution is non-zero. The red contour represents where $k_\perp$ for the slow-wave solution is non-zero. The evanescent region, $k_\perp = 0$ for both waves, is represented by the white contour. The location of the helicon antenna is represented by the thick black line.

5.1. Effect of collisions

Throughout this work, the normalized core power deposition is used as the figure of merit for identifying solutions that are normal modes of the plasma column. The core is defined as the region where $\chi < 0.5$. Figure 6 shows how increasing the collision frequency (ν) reduces the sharpness of the power deposition peaks until they are destroyed. The collision frequency broadens the power deposition peaks because normal mode behavior in the discharge relies on the waves excited from the antenna to interfere constructively on-axis. If the collision frequency is high enough the wave excited by the antenna damps before it can interfere constructively on-axis. To identify the experimentally relevant normal modes the collision frequency will be held at a constant value of $\nu = \omega$, where ω is the driving frequency of the antenna, for the remainder of the analysis. At this value of ν, the higher order k_z modes from the antenna spectrum are damped such that they do not contribute to the core power deposition but the main spectral features can still form normal modes, and structure in the core power deposition plots is still observed in figure 6.

5.2. Identifying experimentally relevant normal modes

Understanding how the antenna couples power to the steady-state plasma is important for predicting the density limitations of the helicon source. Light ion helicon authors have attributed successful high electron density production to excitation of helicon normal modes in the plasma column [9, 12]. In [25] it is described that in a more complicated geometry resonant
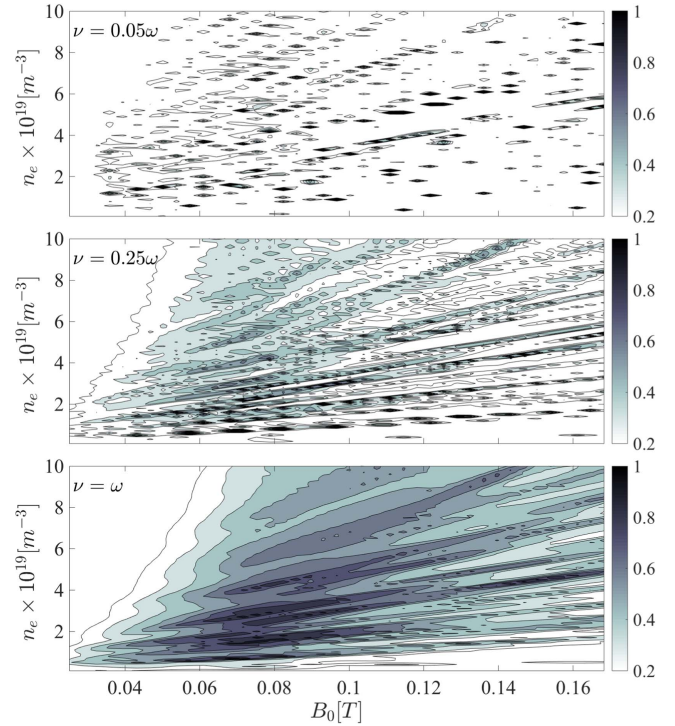

Figure 6. The effect of increasing collision frequency on the contours of core power deposition. Top $\nu = 0.05\omega$, middle $\nu = 0.25\omega$, bottom $\nu = \omega$. The contours show the normalized power deposited in the core.

behavior of the fast-wave does not exist. However, the bounded dispersion relation derived by this approach predicts anti-resonance regimes of the slow-wave. In anti-resonance, the non-resonant mode conversion of the fast-wave to the slow-wave is suppressed. This condition allows the fast-wave to couple increased power into the core plasma. In figure 7 contours of normalized core power deposition are plotted as predicted by the simulation described above. The experimentally relevant parameter space is outlined by the red box. Inside the experimentally relevant parameter space points of maximum core power deposition are identified. These points form 3 distinct lines in $n_e(B_0)$. Since linear behavior in the peak core power deposition is predicted by the bounded dispersion relation given by equation (3), these solutions are referred to as normal mode solutions. The normal mode solutions have the following similar characteristics: (A) significant RF amplitude is present behind the antenna, and (B) reduction of edge power deposition that is not due to inductive coupling. Discussion and an interpretation of these characteristics will be presented in the following sections (5.3 and 5.4). Contours of RF field amplitudes and contours of core power deposition will be compared for a typical normal mode solution, $n_{e_{peak}} = 2.7 \times 10^{19}$ m^{-3} and $I_H = 260$ A, to a simulation with parameters corresponding to a minimum in power deposition, $n_{e_{peak}} = 2.8 \times 10^{19}$ m^{-3} and $I_H = 560$ A. The latter solution is referred to as a TG mode solution because the slow-wave power deposition is more prevalent in these solutions.
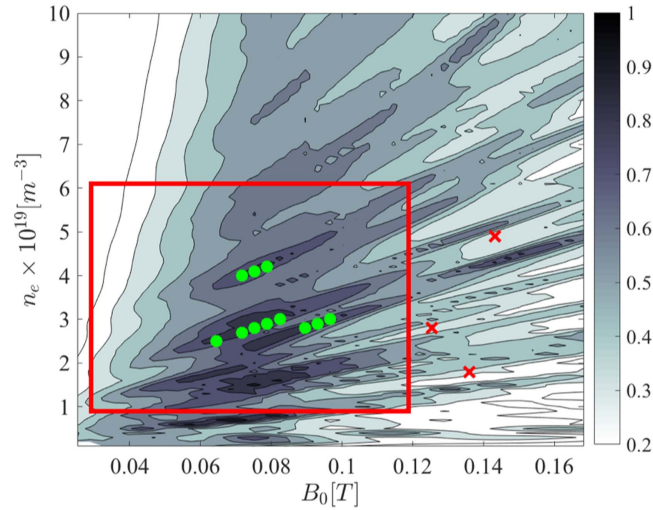
Figure 7. Contours of normalized core power deposition using a constant collision frequency of $\nu = \omega$. The area inside the red square marks the experimentally relevant parameters which will be the focus of the paper. The green circles mark peaks of core power deposition inside of the experimentally relevant parameter space. The red crosses mark areas of minimum core power deposition.

5.3. RF fields

In this section, the RF field (k_z spectrum and $|B_z(r, z)|^2$ variation) of a normal mode solution will be compared to the RF fields of a TG mode solution. Figure 8 shows contours of $|B_z(r, z)|^2$ in real space and radial variation of $\bar{B}_z(r, k_z)$ for the normal mode solution and figure 9 show this data for the TG mode solution. Points along a constant line that are identified as normal modes have similar RF fields as other points along that line. Each constant line of normal mode solutions has an RF field that is different from the other line of normal modes. This behavior is expected since the normal mode solutions must satisfy equation (3) which predicts linear behavior $n_e(B_0)$ if k_z, p_{mi}, R_p, and m are held constant.

The wave solution in real space, figure 8(a), shows that the fast-wave is constrained to the region between the magnetic mirrors, this is due to the fast-wave cut-off present at the large magnetic fields in the magnetic mirror. The presence of these magnetic mirrors creates a cavity for the fast-wave, thus the fast-wave excited by the antenna can be reflected by the mirrors and interfere on-axis if it does not damp or lose energy to slow-wave mode conversion. Figure 8 shows that the plasma spectrum contains waves with negative k_z indicating the fast-wave excited has components traveling in $-\hat{z}$ as well as significant $|B_z|^2$ behind the antenna. Since the $m = +1$ mode of a helical turn antenna primarily excites waves with a positive k_z we can speculate that the waves excited for the normal mode simulations are reflected from the mirror and are allowed to interfere constructively on-axis.

The plasma spectrum of the TG mode solution, shown in figure 9, is dominated by waves with $k_z \approx +20$ m^{-1} which is the dominant k_z feature of the $m = +1$ mode from the antenna vacuum spectrum. Also, there is no significant $|B_z|^2$ present behind the antenna. This indicates the fast-wave excited by the antenna is not effectively reflected by the
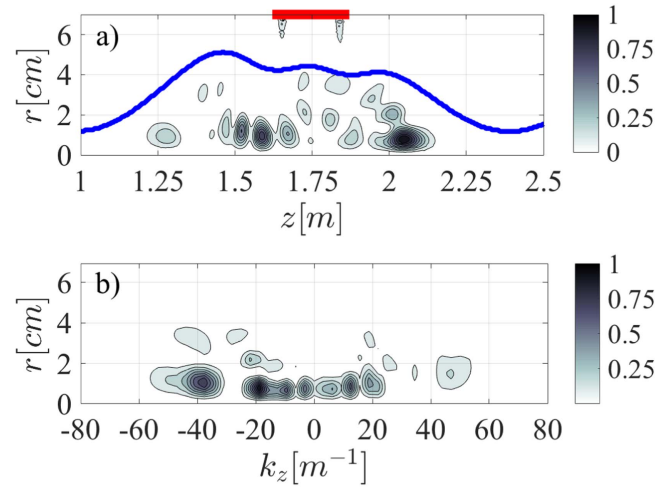

Figure 8. RF field of the normal mode solution. (a) Normalized squared magnitude of the axial component of the RF magnetic field, $|B_z(r, z)|^2$. The blue contour line shows the location of $\chi = 0.5$. The red line shows the location of the helicon antenna. (b) Discrete Fourier transform of the axial component of the RF magnetic field, $\bar{B}_z(r, k_z)$.
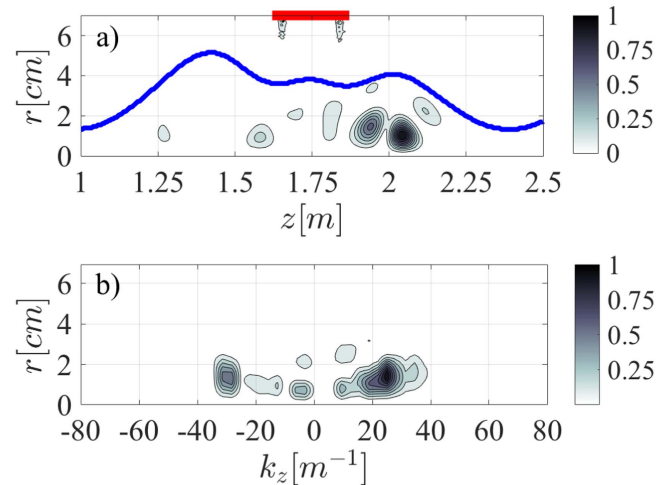

Figure 9. RF field of the TG mode solution. (a) Normalized squared magnitude of the axial component of the RF magnetic field, $|B_z(r, z)|^2$. The blue contour line shows the location of $\chi = 0.5$. The red line shows the location of the helicon antenna. (b) Discrete Fourier transform of the axial component of the RF magnetic field, $\bar{B}_z(r, k_z)$.

magnetic mirror and does not constructively interfere on-axis. In the following section, we show evidence that this is due to the fast-wave mode converting to the slow-wave in the mirror region producing significant edge heating of the plasma.

5.4. Power deposition

Figure 10 shows 2D contours of power loss density from the TG mode solution in Part (a) and the normal mode solution in Part (b). For $k_z = +20$ m^{-1} the dispersion relation allows only the fast-wave to propagate in the core ($\chi < 0.5$) and the slow-wave is constrained to the edge ($\chi \gtrsim 1.0$). Thus, the core power deposition is attributed solely to collisional
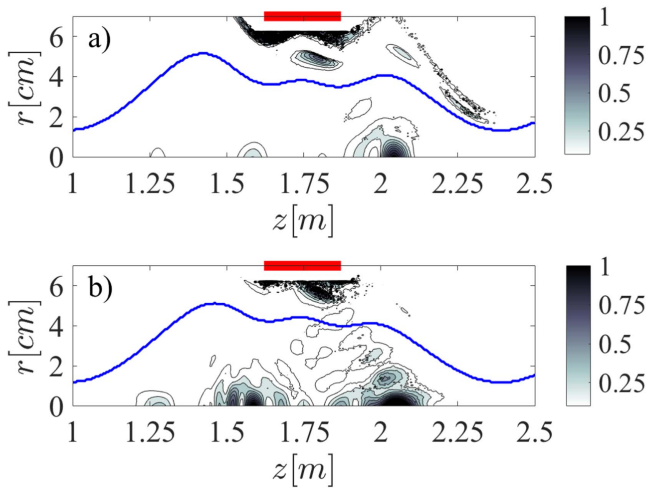
Figure 10. Normalized 2D power loss density for the (a) TG mode solution and (b) normal mode solution. The blue contour line shows the location of $\chi = 0.5$. The red line shows the location of the helicon antenna.

damping of the fast-wave and edge power deposition is attributed to collisional damping of the slow-wave as well as inductive heating. The inductive heating is contained in the region directly under the antenna. Slow-wave heating that is excited by the antenna's near fields is also present under the antenna. However, edge heating that is not located directly under the antenna is attributed to slow-wave excitation through non-resonant mode conversion of the fast-wave [25].

Figure 10 shows that the normal mode solution contains significantly more power deposition in the core, while the TG mode solution contains more power deposition in the edge due to non-resonant mode conversion of the fast-wave. There is significant mode conversion that occurs in the mirror region, which is apparent by the power deposition present there for $\chi > 0.5$. This is consistent with the conclusion from the analysis of the RF field of the TG solution. The fast-wave is not reflected effectively by the mirror since it losses its energy to the slow-wave in this region. This conclusion is also consistent with experimental observations that when there is a jump into the 'helicon-mode' a shift from edge to core dominated power deposition is observed [8, 9]. The integrated core power deposition for the normal mode solution is 43% of the total power deposited in the plasma, while for the TG solution that fraction of power deposition is reduced to 8%. Thus, operating the helicon antenna in a mode where it can effectively excite normal modes significantly increases the amount of core heating that the antenna provides.

6. Conclusion

Throughout this paper, we have presented an electromagnetic 2D axisymmetric model of the helicon antenna on Proto-MPEX. The 2D analytic antenna description represents the realistic antenna geometry as shown by comparison with a self-consistent vacuum simulation of the real geometry of the

3D antenna. The electron density profile used varies axially as a function of the magnetic flux.

With this model, we have identified contours of maximum core power deposition in the parameter space of peak electron density and magnetic field strength that take on a linear trend. The linear trend of normal modes in this parameter space is predicted by equation (3), which requires the plasma parameters to support a normal mode of the fast-wave. The normal mode solutions responsible for these contours in the experimentally relevant parameter space are analyzed. The RF field and power deposition profiles of a normal mode solution are compared to a TG mode solution (point of minimum core power deposition). The normal mode solution seems to have significant negative k_z present in its plasma spectrum, as well as significant fast-wave amplitude in the region behind the antenna $z < 1.75$ m. Since the $m = +1$ azimuthal primarily drives positive k_z fast-waves we conclude that the magnetic mirror reflects the fast-wave propagating towards it which allows the constructive interference of the fast-wave in the plasma core. Therefore the magnetic mirrors act to form a cavity for the fast-wave. In the example of the TG solution, no evidence of significant wave reflection is present. From the contours of power deposition of the TG solution, it is observed that there is significant edge heating present in the mirror region. This edge heating is not present in the mirror region for the case of the normal mode solution. These observations in the power deposition lead to the conclusion that for the case of the TG solution the fast-wave mode converts to the slow-wave in the mirror region, which leads to edge dominated power deposition in these solutions. The normal mode solution couples 43% of the total power into the core, whereas the TG solution only couples 8%. This mechanism could explain why light ion helicon plasmas have only been able to be operated successfully in the presence of a magnetic mirror [7–9, 12, 13].

This model alone cannot predict the mechanisms responsible for the transition into the 'helicon-mode'. Coupling this RF model to a neutral gas and plasma transport simulation is required to shed light on the transition into the 'helicon-mode'. The neutral gas fueling dependence in achieving a 'helicon-mode' plasma is an open question that coupling these simulations would help answer. However, this RF model can be used to optimize the equilibrium state of the 'helicon-mode' plasma in Proto-MPEX. This is done by configuring the magnetic field such that the fast-wave does not mode convert to the slow-wave at the periphery of the plasma so more power is available for density production in the core. A power balance method for predicting the equilibrium density, as proposed by [25], can be used with this RF model to predict electron density limitations of the helicon source.

Acknowledgments

ORCID iDs

P A Piotrowicz ⦿ https://orcid.org/0000-0001-7871-6971
J F Caneses ⦿ https://orcid.org/0000-0001-6123-2081
C Lau ⦿ https://orcid.org/0000-0002-8576-5867
J Rapp ⦿ https://orcid.org/0000-0003-2785-9280

References

[1] Boswell R W 1970 Plasma production using a standing helicon wave *Phys. Lett.* A **33** 457–8

[2] Boswell R W 1984 Very efficient plasma generation by whistler waves near the lower hybrid frequency *Plasma Phys. Control. Fusion* **26** 1147–62

[3] Rapp J, Biewer T, Canik J, Caughman J B O, Goulding R H, Hillis D L, Lore J and Owen L 2013 The development of plasma-material interaction facilities for the future of fusion technology *Fusion Sci. Technol.* **64** 237–44

[4] Rapp J *et al* 2016 The Development of the Material Plasma Exposure Experiment *IEEE Trans. Plasma Sci.* **44** 3456–64

[5] Rapp J *et al* 2017 Developing the science and technology for the material plasma exposure experiment *Nucl. Fusion* **57** 116001

[6] Rapp J, Owen L W, Bonnin X, Caneses J F, Canik J M, Corr C and Lore J D 2015 Transport simulations of linear plasma generators with the B2.5-Eirene and EMC3-Eirene codes *J. Nucl. Mater.* **463** 510–4

[7] Caneses J F and Blackwell B D 2016 Collisional damping of helicon waves in a high density hydrogen linear plasma device *Plasma Sources Sci. Technol.* **25** 055027

[8] Caughman J B O *et al* 2017 Plasma source development for fusion-relevant material testing *J. Vac. Sci. Technol.* A **35** 03E114

[9] Goulding R H *et al* 2017 Progress in the development of a high power helicon source for the materials plasma exposure experiment *Fusion Sci. Technol.* **72** 588–94

[10] Sakawa Y, Takino T and Shoji T 1999 Contribution of slow waves on production of high-density plasmas by $m = 0$ helicon waves *Phys. Plasmas* **6** 4759

[11] Light M, Chen F F and Colestock P L 2001 Low frequency electrostatic instability in a helicon plasma *Phys. Plasmas* **8** 4675–89

[12] Mori Y, Nakashima H, Baity F W, Goulding R H, Carter M D and Sparks D O 2004 High density hydrogen helicon plasma in a non-uniform magnetic field *Plasma Sources Sci. Technol.* **13** 424–35

[13] Yoshitaka M, Hideki N, Baity F W, Goulding R H, Carter M D and Sparks D O 2006 Focusing magnetic field contribution for helicon plasma on Mini-RFTF *Thin Solid Films* **506–507** 583–7

[14] Loewenhardt P K, Blackwell B D, Boswell R W, Conway G D and Hamberger S M 1991 Plasma production in a toroidal heliac by helicon waves *Phys. Rev. Lett.* **67** 2792–4

[15] Molvik A W, Ellingboe A R and Rognlien T D 1997 Hot-electron production and wave structure in a helicon plasma source *Phys. Rev. Lett.* **79** 233–6

[16] Blackwell D D, Madziwa T G, Arnush D and Chen F F 2002 Evidence for Trivelpiece–Gould modes in a helicon discharge *Phys. Rev. Lett.* **88** 145002

[17] Breizman B and Arefiev A 2000 Radially localized helicon modes in nonuniform plasma *Phys. Rev. Lett.* **84** 3863–6

[18] Chen F F and Blackwell D D 1999 Upper limit to Landau damping in helicon discharges *Phys. Rev. Lett.* **82** 2677–80

[19] Kline J L, Scime E E, Boivin R F, Keesee A M, Sun X and Mikhailenko V S 2002 rf absorption and ion heating in helicon sources *Phys. Rev. Lett.* **88** 195002

[20] Niemi K and Krämer M 2008 Helicon mode formation and radio frequency power deposition in a helicon-produced plasma *Phys. Plasmas* **15** 073503

[21] Shamrai K P and Taranov V B 1996 Volume and surface rf power absorption in a helicon plasma source *Plasma Sources Sci. Technol.* **5** 474–91

[22] Arnush D 2000 The role of Trivelpiece–Gould waves in antenna coupling to helicon waves *Phys. Plasmas* **7** 3042

[23] Chen F F and Curreli D 2013 Central peaking of magnetized gas discharges *Phys. Plasmas* **20** 057102

[24] Curreli D and Chen F F 2011 Equilibrium theory of cylindrical discharges with special application to helicons *Phys. Plasmas* **18** 113501

[25] Shamrai K P 1998 Stable modes and abrupt density jumps in a helicon plasma source *Plasma Sources Sci. Technol.* **7** 499–511

[26] Carter M D, Baity F W, Barber G C, Goulding R H, Mori Y, Sparks D O, White K F, Jaeger E F, Chang-Díaz F R and Squire J P 2002 Comparing experiments with modeling for light ion helicon plasma sources *Phys. Plasmas* **9** 5097–110

[27] Shamrai K P and Taranov V B 1994 Resonance wave discharge and collisional energy absorption in helicon plasma source *Plasma Phys. Control. Fusion* **36** 1719–35

[28] Degeling A W, Sheridan T E and Boswell R W 1999 Intense on-axis plasma production and associated relaxation oscillations in a large volume helicon source *Phys. Plasmas* **6** 3664

[29] Degeling A W, Sheridan T E and Boswell R W 1999 Model for relaxation oscillations in a helicon discharge *Phys. Plasmas* **6** 1641

[30] Arnush D and Chen F F 1998 Generalized theory of helicon waves: II. Excitation and absorption *Phys. Plasmas* **5** 1239

[31] Cho S 2009 Eigenmode dispersion relations in radially inhomogeneous helicon plasmas *Phys. Plasmas* **16** 063504

[32] Swanson D G 1989 *Plasma Waves* (Philadelphia, PA: Institute of Physics Publishing) p 434

[33] Mouzouris Y and Scharer J E 1996 Modeling of profile effects for inductive helicon plasma sources *IEEE Trans. Plasma. Sci.* **24** 152–60

[34] Caneses J F, Blackwell B D and Piotrowicz P 2017 Helicon antenna radiation patterns in a high density hydrogen linear plasma device *Phys. Plasma* **24** 113513